

Investigation of air bubble behavior after gas embolism events induced in a microfluidic network mimicking microvasculature

Mohammad Mahdi Mardanpour^{1,*}, Ayyappasamy Sudalaiyadum Perumal^{1,*}, Zahra Mahmoodi¹,

Karine Baassiri¹, Gala Montiel Rubies¹, Kenneth M. LeDez², Dan V. Nicolau¹

¹Department of Bioengineering, Faculty of Engineering, McGill University, Montreal, Québec, H3A
0E9, Canada

²Faculty of Medicine, Memorial University, Health Sciences Centre, St. John's, Newfoundland and
Labrador, A1C 5S7, Canada

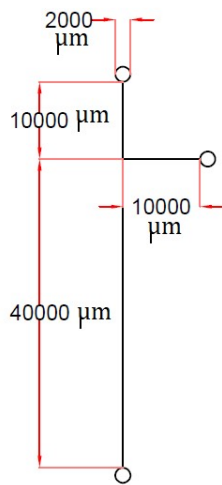
*These authors contributed equally to this work.

SUPPLEMENTARY INFORMATION

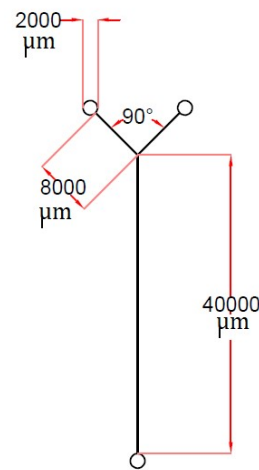
1. Dimensions of the mimicked microvasculature

The dimensions of the mimicked microvasculature, namely linear T-junction channels, linear Y-junction channels, and bifurcating honeycomb microchannels, are illustrated in Fig. S1. The linear channels presented two types of junctions and three different widths, namely 20 μm , 40 μm and 60 μm . While the honeycomb bifurcation network had a constant width (30 μm) and varying bifurcation angles (30, 60 and 90 $^\circ$).

(A)



(B)



(C)

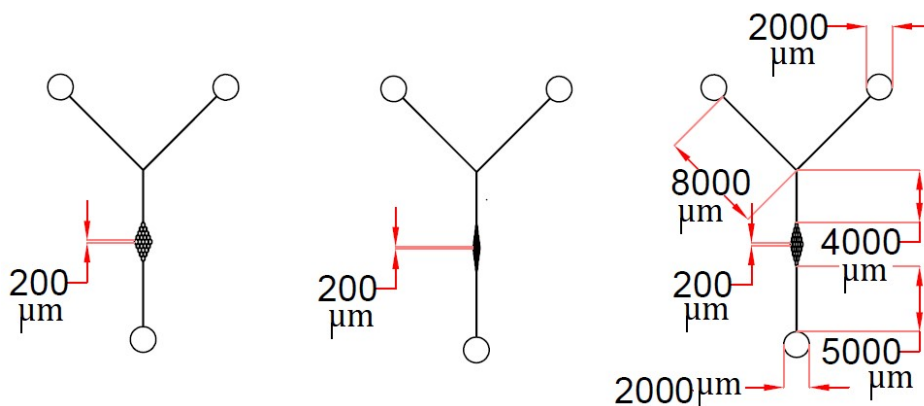


Fig. S1 Dimensions of the mimicked microvasculature. (A) T-junction single microchannel; (B) Y-junction single microchannel; (C) Honeycomb-like bifurcation microvascular channel.

2. Master fabrication

The microvasculature designs were created using Fusion 360 and printed on a mylar sheet to fabricate a photomask (made by CAD/Art Services, Inc.). A SU-8 negative photoresist 2050 (Kayaku Advanced Materials, Inc.) layer with a 40 μm thickness was coated on 4-inch silicon wafers (Ultra-flat single-side polished silicon substrates, 1000 μm thickness, Alpha Nanotech Inc.) by a spin coater (WS-650-23 B spin coater, Laurell Technologies Corporation). The silicon wafer, photomask alignment and UV exposure were performed using a mask aligner system (OAI, Hydralign Series 200). Coating the photoresist layer was fulfilled using a spin coater at 3600 rpm. The soft baking of the spin-coated silicon wafer was done at 65 and 95 $^{\circ}\text{C}$ for 3 and 6 min, respectively. Then, the photomask was placed onto the photoresist spin-coated silicon wafer and UV-exposed for 55 seconds. The UV light intensity was 3.1 mWcm^{-2} . After UV exposure, the post baking process was done at 65 and 95 $^{\circ}\text{C}$ for 1 and 6 min, respectively. The unexposed surface of the photoresist layer was then removed by dissolving it with SU-8 developer (Kayaku Advanced Materials, Inc.). The developing time was 1 min. The thickness ($40 \pm 3 \mu\text{m}$) of the developed photoresist layer was measured by a profilometer (The Bruker Dektak XT contact profilometer, Bruker Inc.). Finally, a silanization surface treatment was done using chlorotrimethylsilane for 24 h to improve the bonding in the interface between mineral and organic components.¹ The schematic of the masters' fabrication procedure and PDMS replication of the mimicked microvasculature are shown in Fig. S2.

3. Polydimethylsiloxane (PDMS) replication moulding

Polydimethylsiloxane (PDMS, Sylgard Silicone elastomer 184, Dow Corning Corp. Midland, MI.) and curing agent were mixed in a 10:1 ratio (weight by weight). PDMS mixture was poured onto the fabricated master and then degassed to remove the air bubbles. The curing process was carried out overnight at 60 $^{\circ}\text{C}$ in an oven. After curing, the PDMS with microchannels networks was removed from the silicon wafer, and the holes for inlets and outlets were punched (1.5mm diameter punctures were used). The PDMS was treated using a plasma cleaner (PDC-32G, Harrick plasma) to form an

irreversible bond, and then a glass cover slip was used to seal the microfluidic channels. The locked microfluidic devices were then used for experiments.

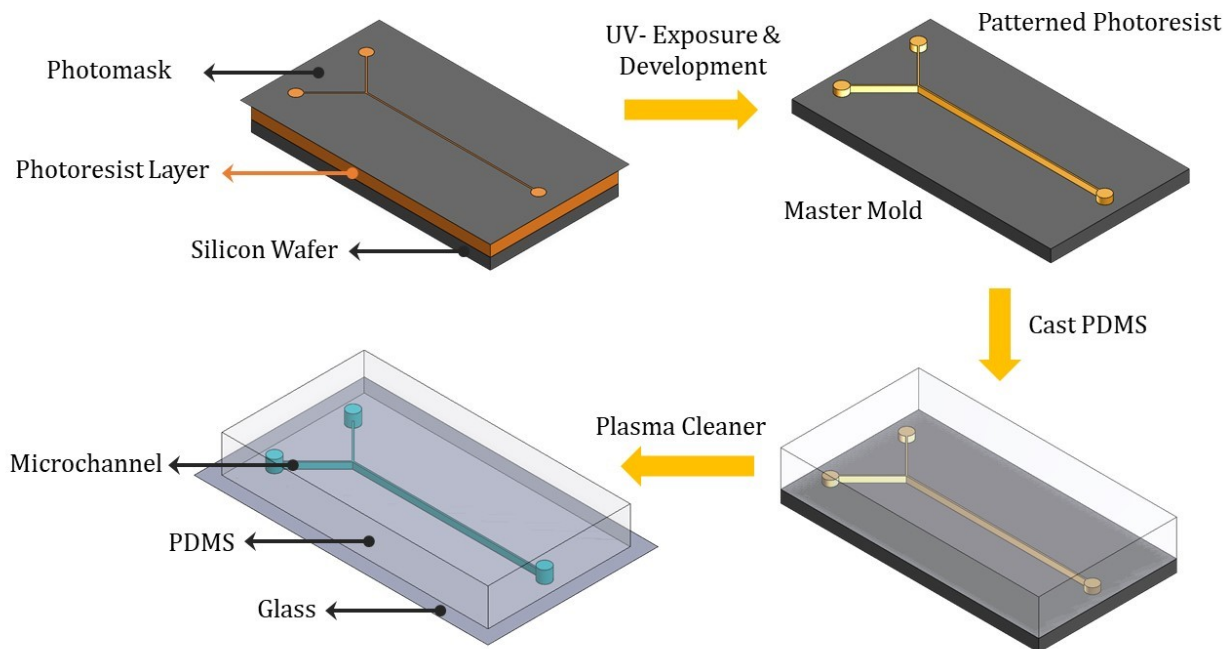


Fig. S2 Schematic of the masters' fabrication and the replication process of the microvasculature devices.

4. Measurement of the viscosity and surface tension of the synthesized fluids

The working fluids were prepared according to the procedure mentioned in the work of Brookshier and Trabell.² The xanthan gum-based haematocrit equivalent has also been used in several other studies^{2,3} as a synthetic replacement of haematocrit equivalent fluids for PDMS-based microfluidics studies. To demonstrate their similarity with human blood characteristics, their viscosity (Table S1), surface tension (Table S2) and contact angle were measured (Table S3). The viscosities of the working fluids were measured and reported at the shear rate of 120 s^{-1} and 20°C by a rheometer (Modular Compact Rheometer, MCR 302e, Anton Paar). The detailed results are shown in Fig. S3.

Table S1. The viscosity of the working fluids versus the viscosity of real blood was reported in the work of Brookshier and Trabell.²

Fluid Viscosity (cp)	Human Blood* ⁴	Working Fluid with equivalent haematocrit concentration at 20°C
Plasma at 37 °C (0% haematocrit concentration)	1.1	1.0
Whole blood with 20% haematocrit concentration	2.1	2.5
Whole blood with 46% haematocrit concentration	5.7	6.0

*The viscosities of the working fluids were reported at the shear rate of 120 s⁻¹.

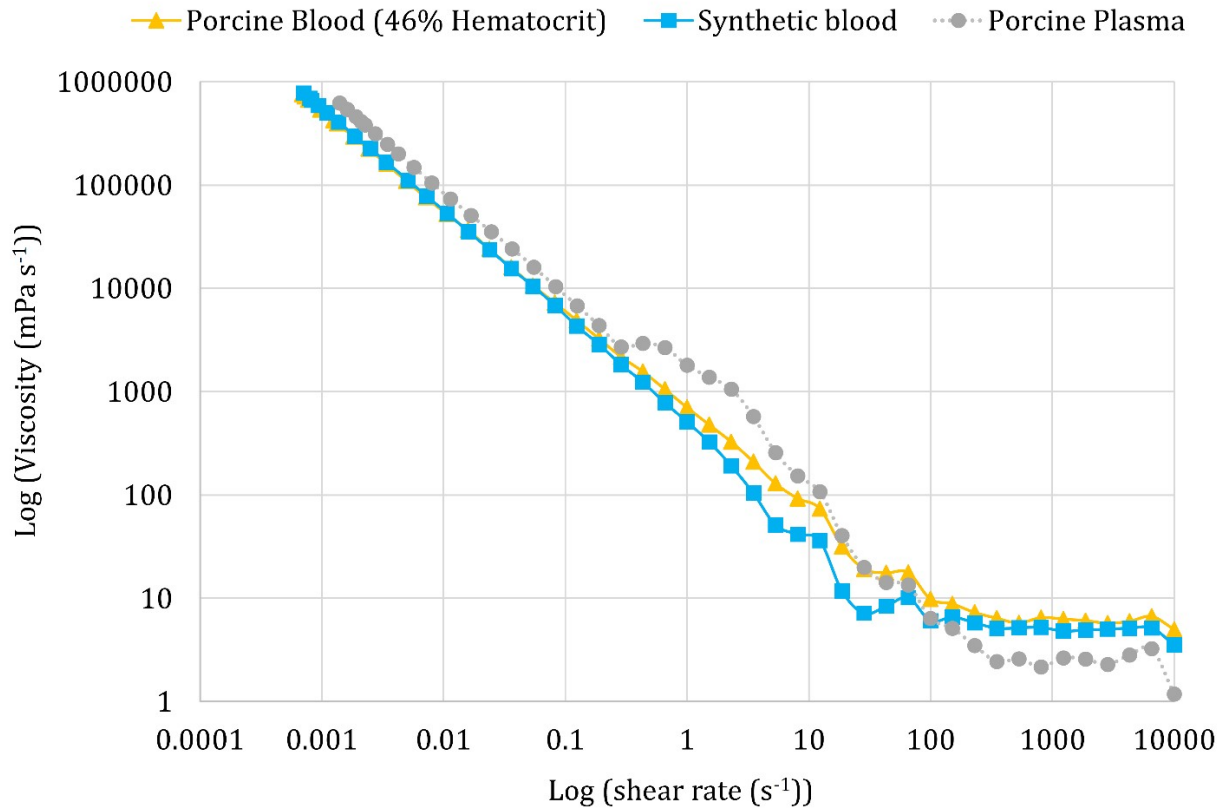


Fig. S3 The obtained data during viscosity measurement of working fluids and porcine blood (N=3).

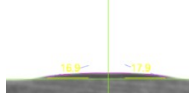
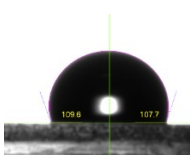
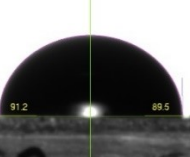
The surface tension and contact angle were measured by Ramé-hart Model 90 Goniometer / Tensiometer (Ramé-hart Instrument co.).

Table S2. The surface tension of human blood at different haematocrit equivalent versus the surface tension of working fluids.

Fluid surface tension (mN/m)	Human blood ^{5,6}	Working fluid with equivalent haematocrit concentration at 20°C
Plasma (0% haematocrit concentration)	52	56.95
Whole blood with 46% haematocrit concentration	54	48.97

The contact angle of the synthesized fluids versus the contact angle of the real blood.

Table S3. The surface tension and contact angle of the working fluids and porcine blood (N=10).

Water – Glycerol	Water	Synthetic blood	Porcine plasma	Porcine 46% hematocrit
Surface Tension σ				
Dyne/cm (mN/m)	56.95	48.97	53.24	47.26
Contact angle on the glass slide				
θ	17.00	35.50	24.50	20.90
Contact angle on PDMS				
θ	108.60	90.30	70.00	98.50

5. Microscopy images

The microscopy image panel for varying flow patterns for all tested air-to-liquid flow ratios, ranging from 10 to 100, for both junction types and all fluids, are presented in Supplementary Information Figs. S4 to S6.

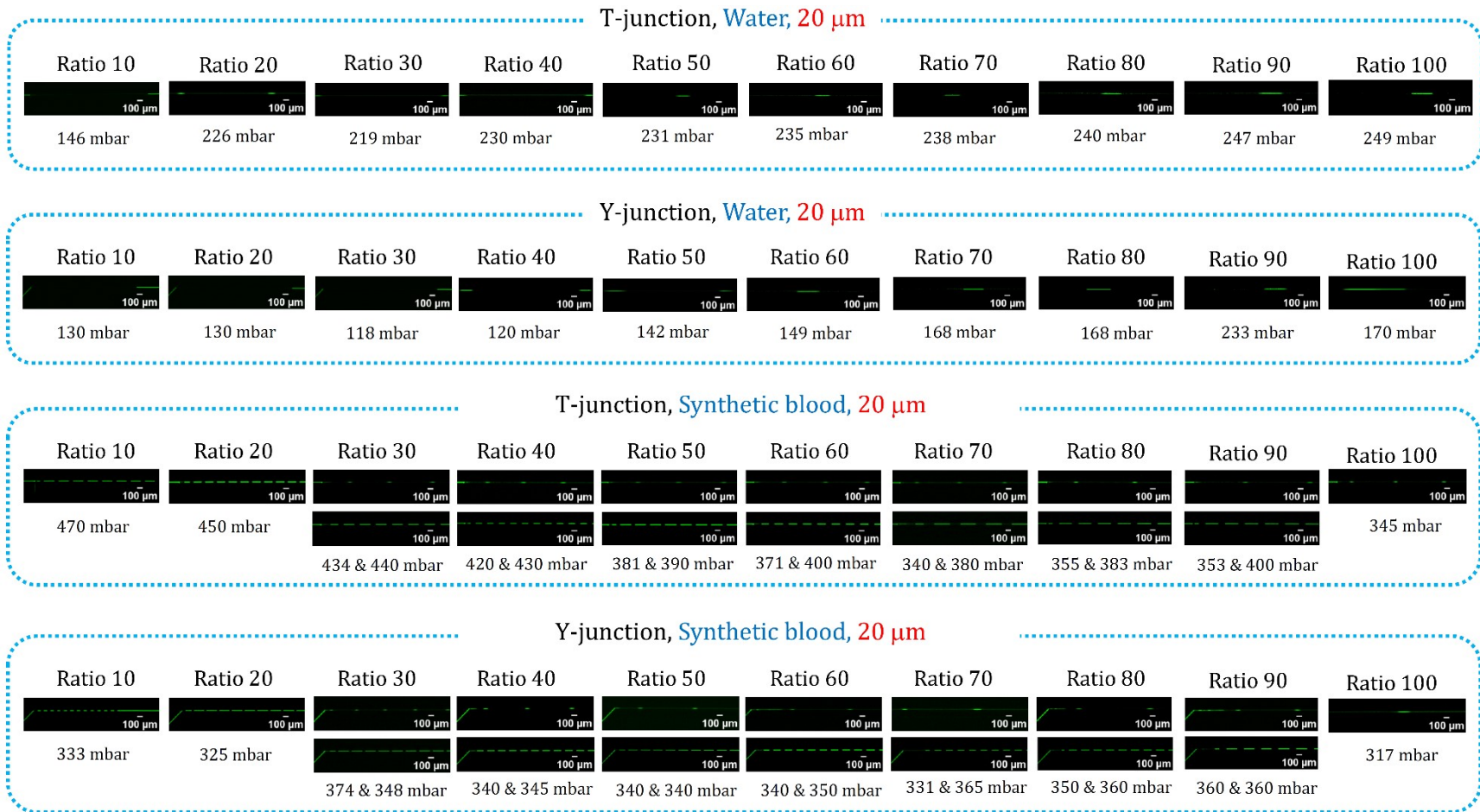


Fig. S4. Microscopic images of the flow patterns of air bubbles and liquid slugs in T-junction and Y-junction of 20 μm channel width across different air-to-liquid ratios for the water and synthetic blood.

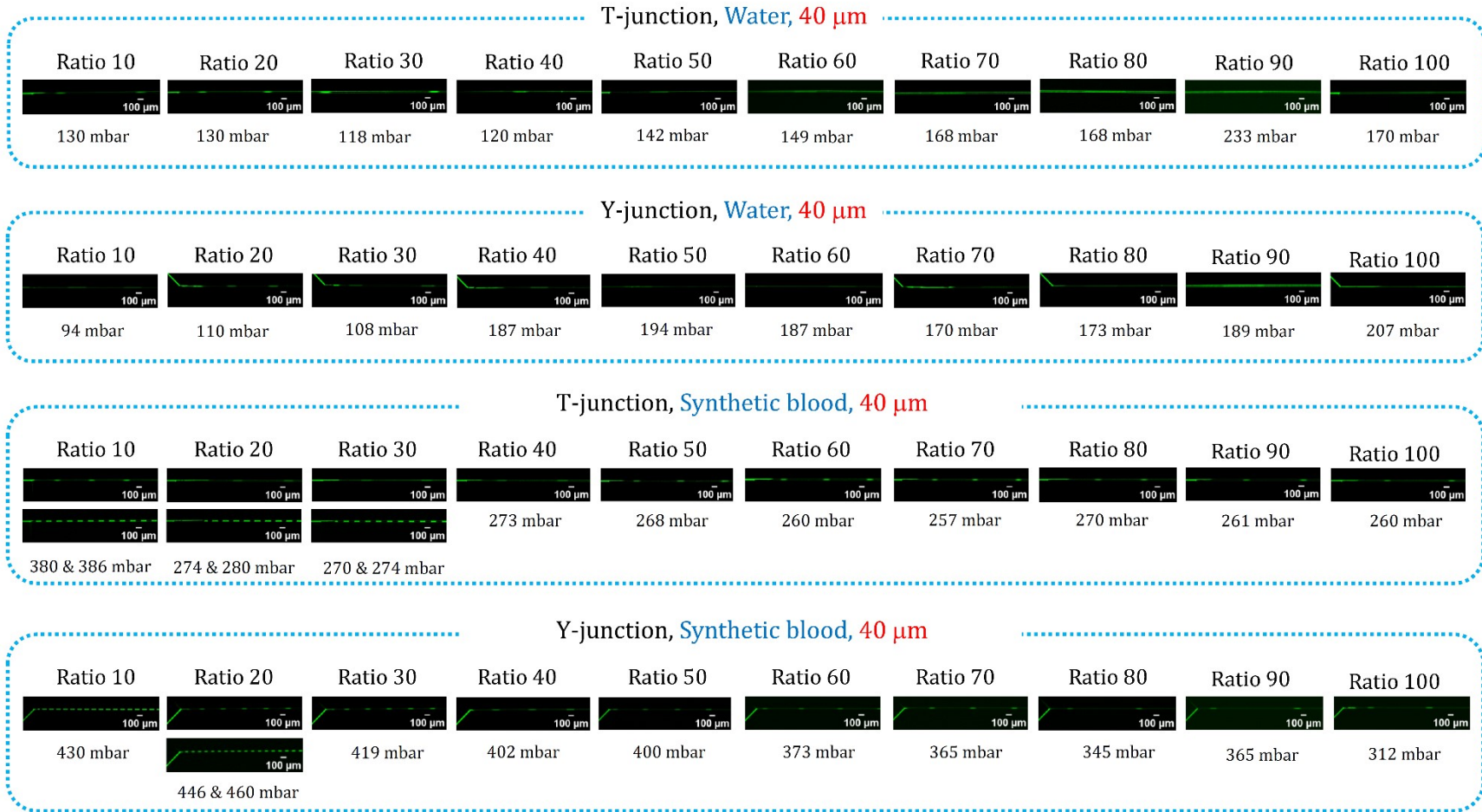


Fig. S5. Microscopic images of the flow patterns of air bubbles and liquid slugs in T-junction and Y-junction of 40 μm channel width across different air-to-liquid ratios for the water and synthetic blood.

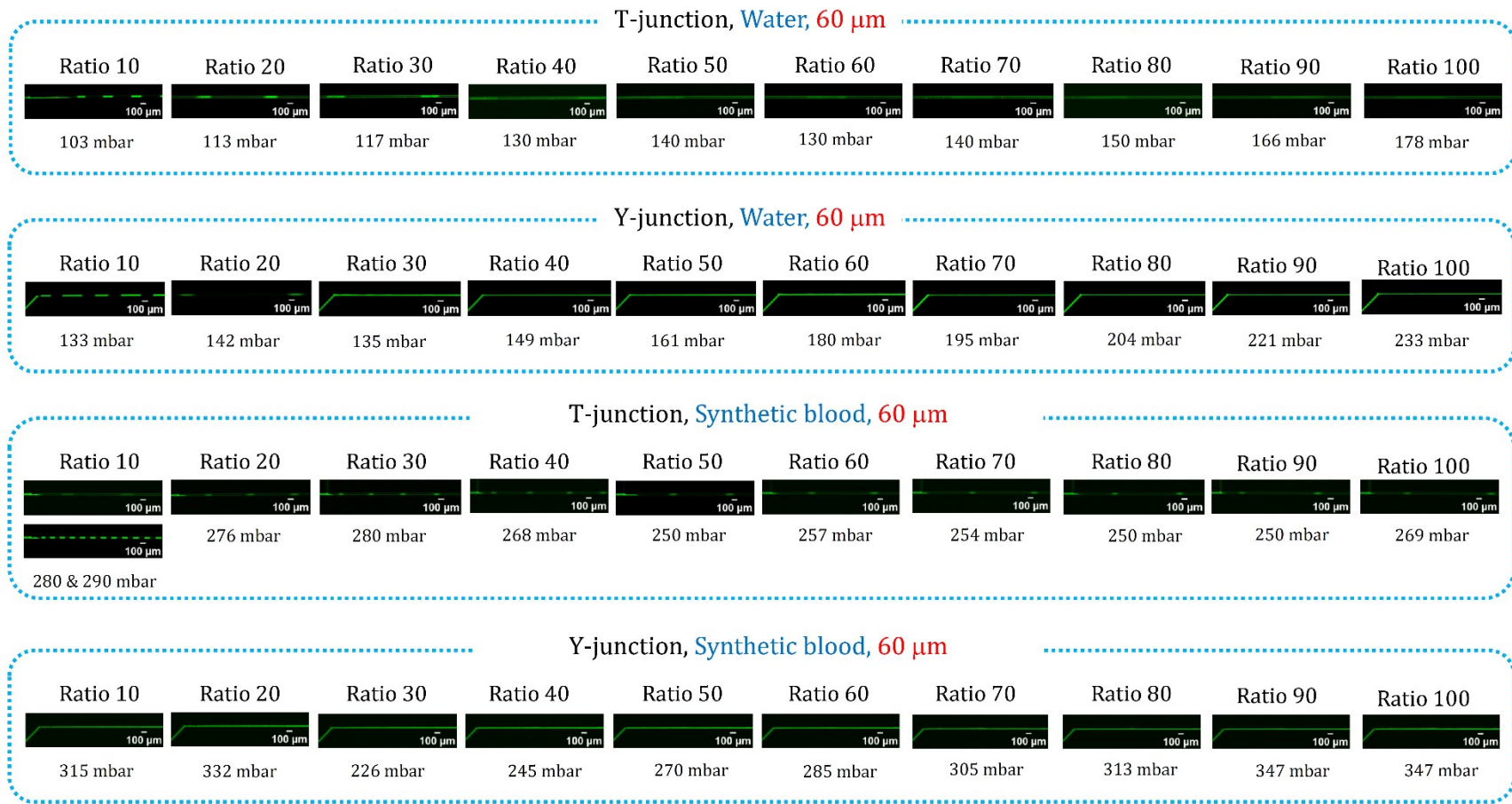


Fig. S6. Microscopic images of the flow patterns of air bubbles and liquid slugs in T-junction and Y-junction of 60 μm channel width across different air-to-liquid ratios for the water and synthetic blood.

6. Variation of the fluid pressure drop across the channel.

The variation of the pressure drop in channels with both T and Y-junctions for water and synthetic blood for different air-to-liquid ratios is presented in Fig. S7. During the monitoring of the pressure drops for an extended period (which was 140, 50, and 30 min for the 20, 40 and 60 μm channels, respectively), two pressure ranges were observed, namely (i) a highly dynamic region, at the start of the injection of the liquid and air, where the hydraulic pressure raised considerably, as shown in Fig. S7, and then (ii) a stabilized region, during which the pressure values reached constant levels, as presented in Fig. S7 (and further detailed in Supplementary Information, Figs. S8 to S13). In the highly dynamic region, the pressure values were up to twice the values compared to the constant region (Fig. S7). In the stabilized region of the pressure drop, which is the focus of the present study, two different distributions of bubble and total slug lengths were observed: (i) a more uniform-sized total slug and (ii) a non-uniform total slug sizes. Figs. S4 to S6 and Movie. S2 show the microscopic images of these two size distributions in corresponding air-to-liquid ratios. For uniformly sized total slugs, the air bubbles and liquid slugs traversed harmonically along the channel without a significant difference in the length of the moving bubbles or liquid slugs (referred to here as harmonic motion). This pattern was observed in most air-to-liquid ratios for flows in 20 μm channels. For 40 and 60 μm channels, the harmonic motion of the bubble occurred just in a few instances when the air-to-liquid ratios were lower. For higher air-to-liquid ratios in the Y-junction, non-uniform distributed lengths of the total slugs were observed.

Fig. S7 presents general trends of the pressure drop measured for varying air-to-liquid ratios, derived from independent experiments ($1700 \leq n \leq 44000$, and $3500 \leq n \leq 198000$ measurements, for the water and synthetic blood, respectively). High variations (longer vertical lines for standard deviations in Fig. S7) correspond to irregular flow patterns resulting from the resistance developed due to air bubble entrapment in the channels, which is phenomenologically similar to gas embolism events. Conversely, smaller variations correspond to more uniform flow patterns and predictable

characteristics of the total slugs, i.e., successive displacement of air bubbles and liquid phases without considerable stagnation. The bubbles resulting from this seamless displacement are denominated as Taylor bubbles (or continuously displacing bubbles).⁷ The pressure drop in a straight channel with Taylor flow is a function of the length of liquid slugs, bubble lengths, their velocity, channel width, and fluid viscosity.⁸ Therefore, to interpret the experimental results of the pressure drop, factoring in the variation of the mentioned parameters is essential.⁹

A comparison of the graphs in Fig. S7 suggests that the effect of fluid viscosity has a considerably higher impact on the pressure drop variations than other parameters, such as the fluid flow velocity, air-to-liquid ratio, flow pattern, and channel width. The channels accommodating fluid flows characterized by higher viscosity exhibit higher pressure drops than the ones with a lower viscosity. For instance, in T-junctions, the higher viscosity of the synthetic blood compared with the water viscosity translates into a generally higher pressure drop (Fig. S7B) compared to that for water (Fig. S7A). A similar pattern was observed with Y-junctions, as shown in Fig. S7C and Fig. S7D.

Apart from the liquid viscosity, the hydraulic resistance of the channels with T-junction affects considerably more the pressure drop compared to those with Y-junction (Fig. S7A and S7B). Furthermore, in T junctions with 20 μm channel width exhibits the highest hydraulic resistance, followed by the channels with 40 μm and 60 μm widths, and consequently, the highest pressure drop. An increase in the channel width decreased the pressure drop, and consequently, the 40 and 60 μm channels have a lower pressure drop than the 20 μm channels. As a result, the movement of the air bubble in 20 μm channels is particularly challenging, with the highest propensity for halting. The application of Hagen–Poiseuille relationship (Eq. 1),¹⁰ stating that an increase in the liquid viscosity increases the air pressure (or pressure drop), can be observed by comparing Fig. S7A and S7B. The findings are in line with previously published results.⁹ The Hagen–Poiseuille correlation is further detailed in Eq. 1:

$$\Delta P = \frac{128 \times \mu \times L \times Q}{\pi \times d_H^4} \quad \text{Eq. 1}$$

Where ΔP represents pressure drop (Pa), μ denotes the dynamic viscosity (kg m s^{-1}), L indicates the length of the channel (m), Q is the fluid flowrate ($\text{m}^3 \text{s}^{-1}$), and finally d_H is the hydraulic diameter of the channel (m).

Similar to T-junctions, Y-junctions also presented a higher hydraulic pressure for the synthetic blood than water. However, unlike the T-junctions, Y-junctions, which are the default geometry in the vascular system, presented a different trend with respect to the pressure drop. The channel with larger widths (namely $40 \mu\text{m}$) showed a higher pressure drop compared to the lower channel widths ($20 \mu\text{m}$), suggesting a different and unpredictable behaviour of flow in the presence of gas bubbles dependent on the junction type. In a similar study, variations in pressure drops within a channel with T-junction were examined.¹¹ The study found that a higher pressure drop can be as a result of increasing the channel width or by increasing the fluid flow rate, which, in turn, affects the flow pattern of bubbles within the channel. In our study, while Eq. 1 clearly demonstrates the direct impact of viscosity (μ) and flow rate (Q) (Fig S7A and S7B), another factor not considered in the Hagen–Poiseuille relation is the movement patterns of the bubbles in channel of different width. This can be attributed to the unpredictable behavior in pressure drop with $40 \mu\text{m}$ channels observed to be higher than in the $20 \mu\text{m}$ channels. Following the above observation of anomaly, it is obvious to expect the pressure drop to be highest in $60 \mu\text{m}$ channel with Y-junctions among the studied widths, however, it was the not the case. The possible explanation is in $60 \mu\text{m}$ channels, the flow pattern was stratified, and the layer of the gas moved parallelly along the layer of the liquid for both water and the synthetic fluid. As a result, only a linear variation of the air pressure for different air-to-liquid ratios was observed for Y-junctions (green lines in Fig. S7C and S7D). This observation emphasizes on the fact that was not earlier studied with invitro experiments, but detailed here stating that the patterns of bubble movement could be critical for the pressure drop.

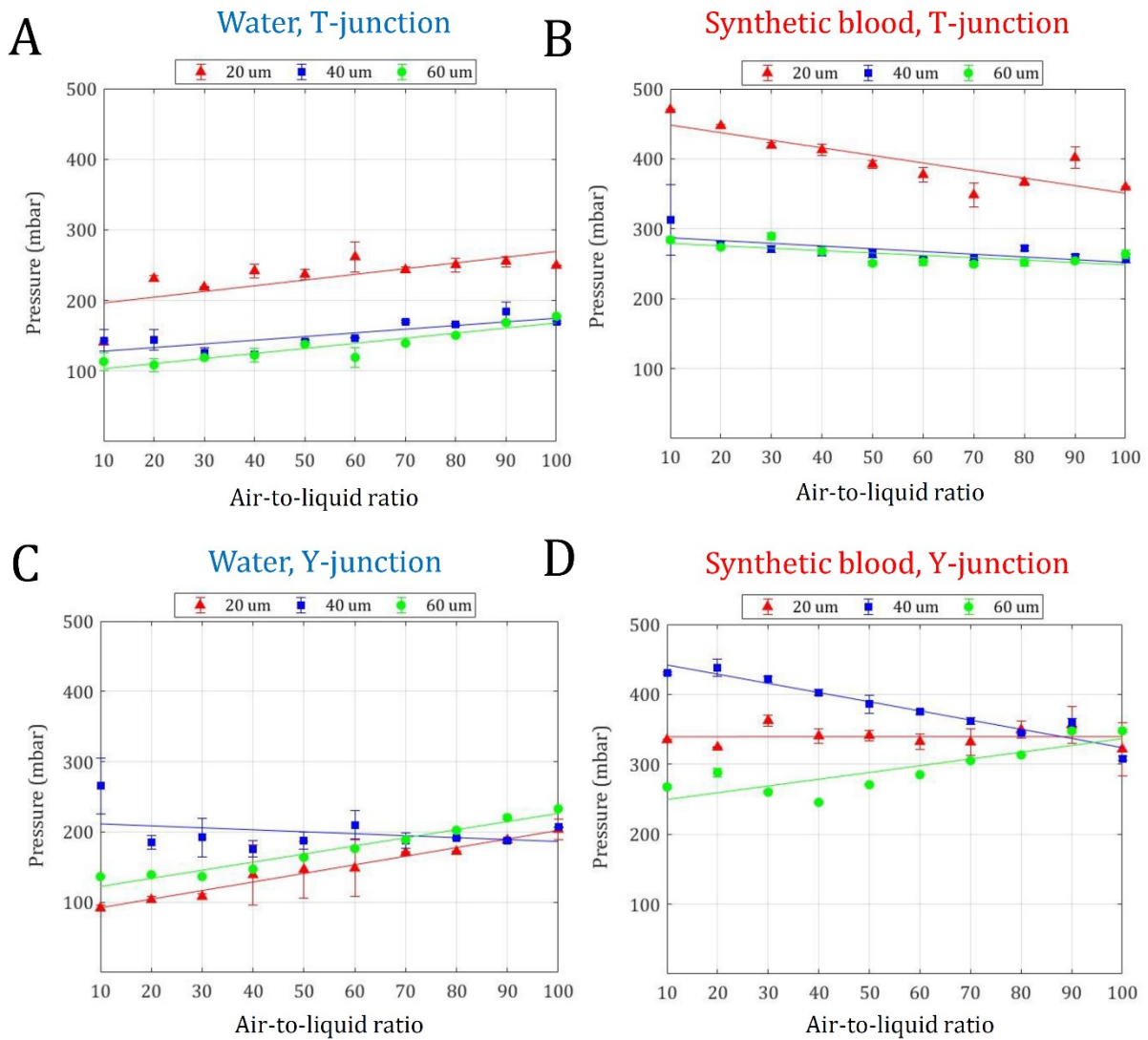


Fig. S7 Graphs of the measured air pressure for different air-to-liquid ratios for different viscosity and channel junctions. A. water and T-junction channel; B. the synthetic blood and T-junction channel; C. water and Y-junction channel; D. the synthetic blood and Y-junction channel. The standard deviation represents the pressure variation of the injected airflow measured by the pressure sensor, with larger values representing larger fluctuations in the pressure of the air.

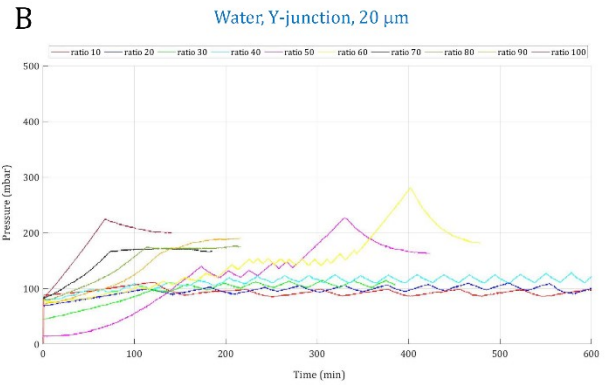
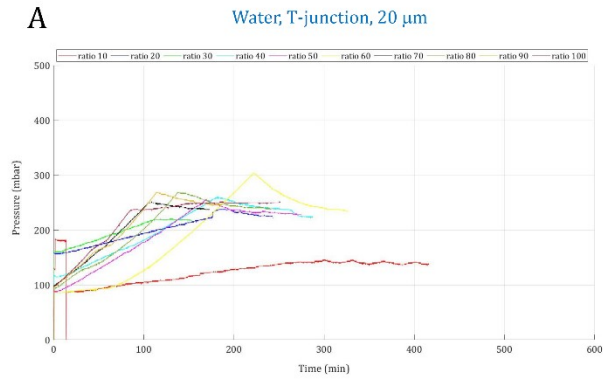


Fig. S8 Pressure evolution inside channels with 20 μm width for water. A. T-junction, B. Y-junction.

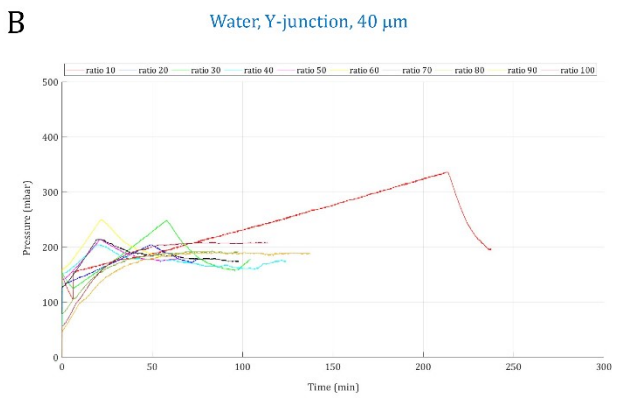
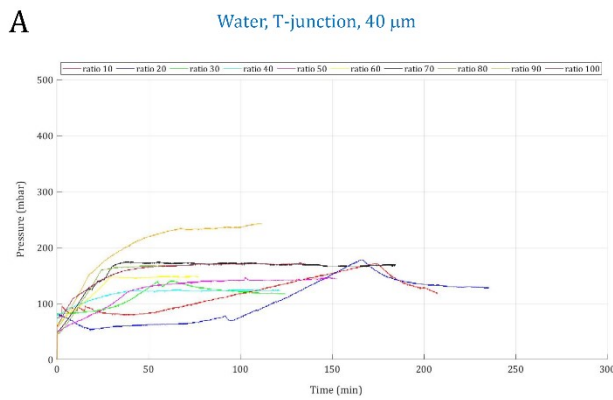


Fig. S9 Pressure evolution inside channels with 40 μm width for water. A. T-junction, B. Y-junction.

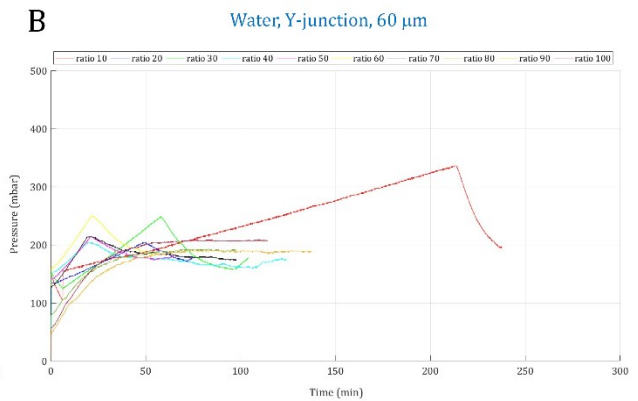
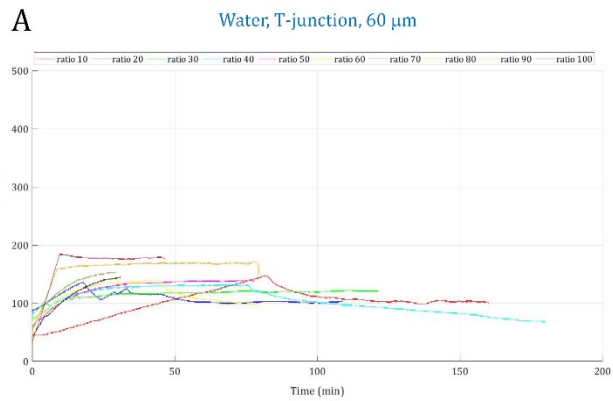


Fig. S10 Pressure evolution inside channels with 60 μm width for water. A. T-junction, B. Y-junction.

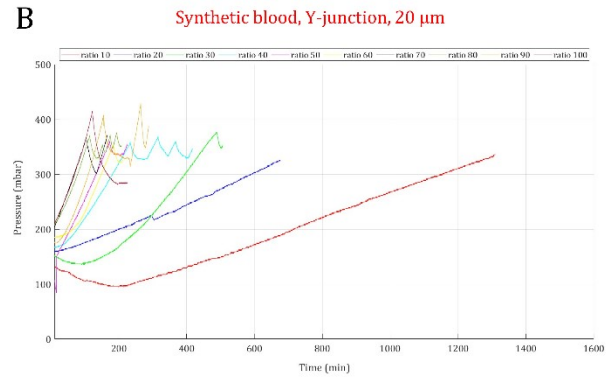
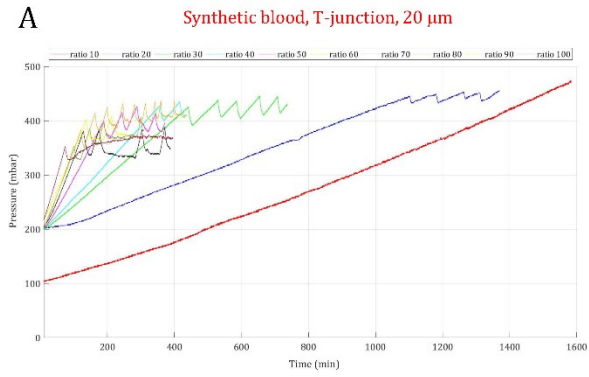


Fig. S11 Pressure evolution inside channels with 20 μm width for the synthetic blood. A. T-junction, B. Y-junction.

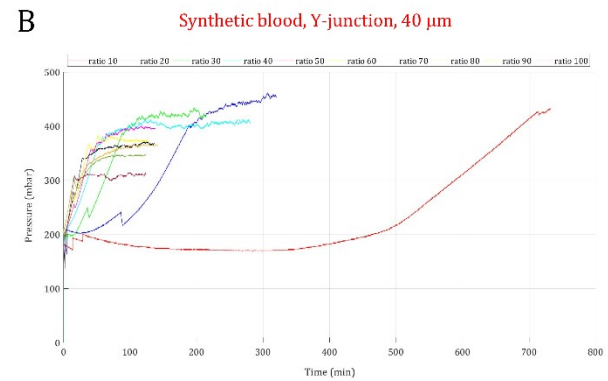
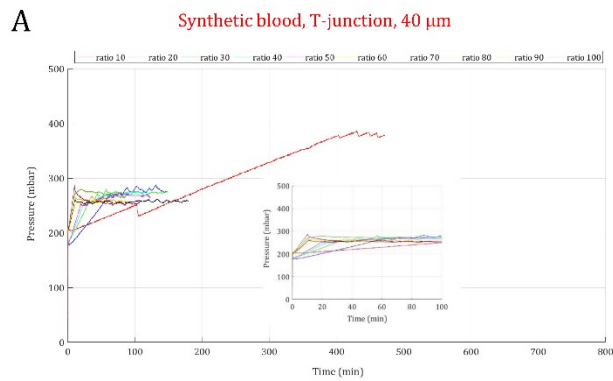


Fig. S12 Pressure evolution inside channels with 40 μm width for the synthetic blood. A. T-junction, B. Y-junction.

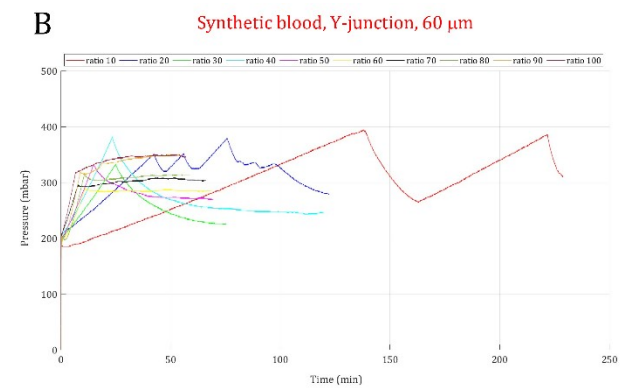
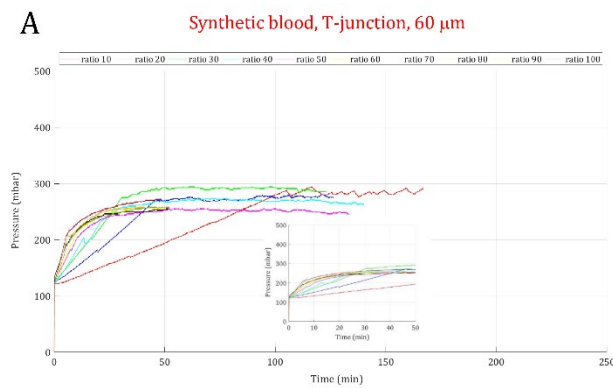


Fig. S13 Pressure evolution inside channels with 60 μm width for the synthetic blood. A. T-junction, B. Y-junction.

7. Length of the liquid slug and histogram of the bubble length in T and Y-junctions

A representative panel of the length of the liquid slug and histogram of the bubble length observed with different flow ratios and equivalent concentrations of haematocrit for both T-junction and Y-junction is shown below.

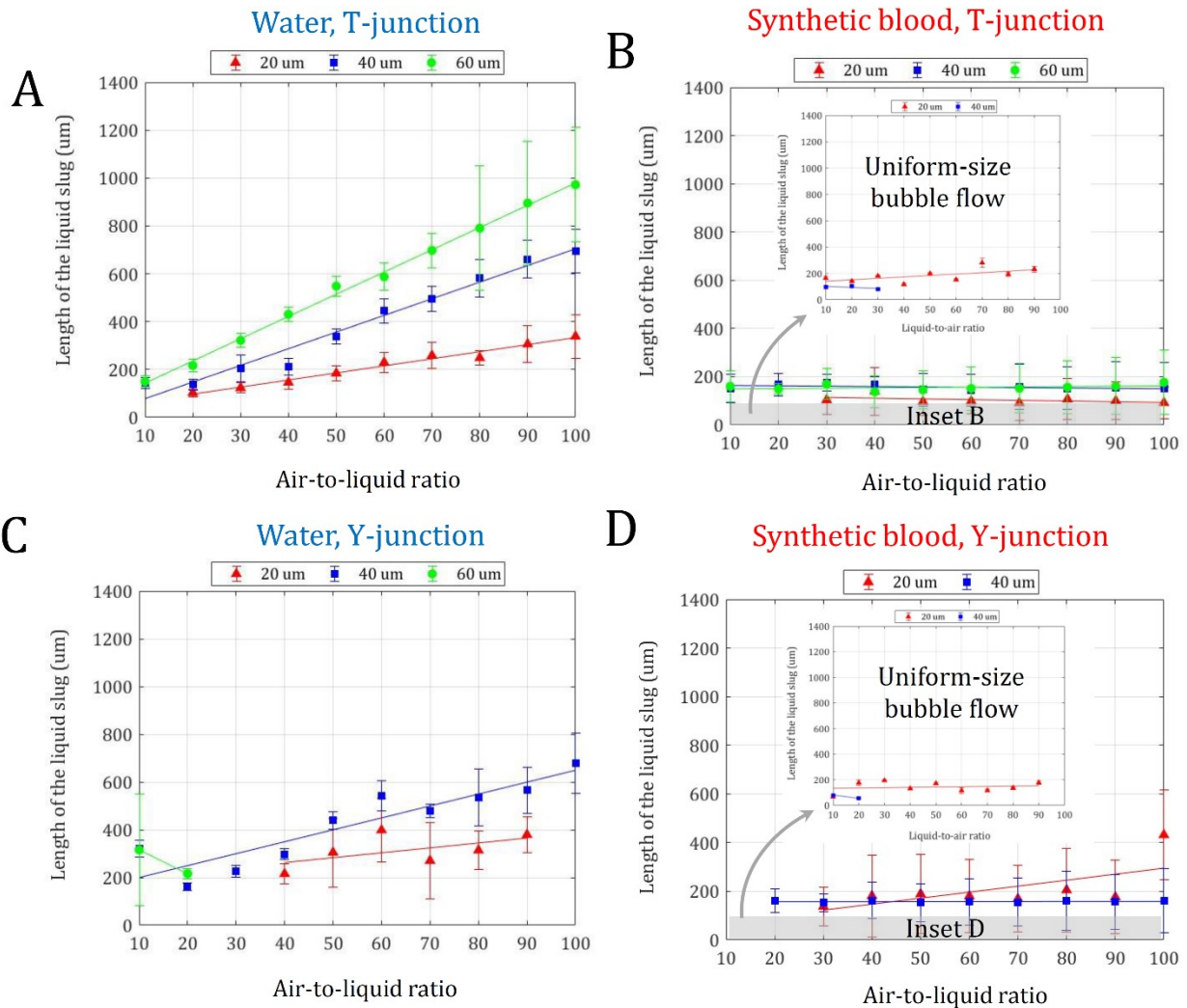


Fig. S14 Length of the liquid slugs in T-junction and Y-junction channels across different air-to-liquid ratios for the water and synthetic blood.

8. Distribution of bubble lengths

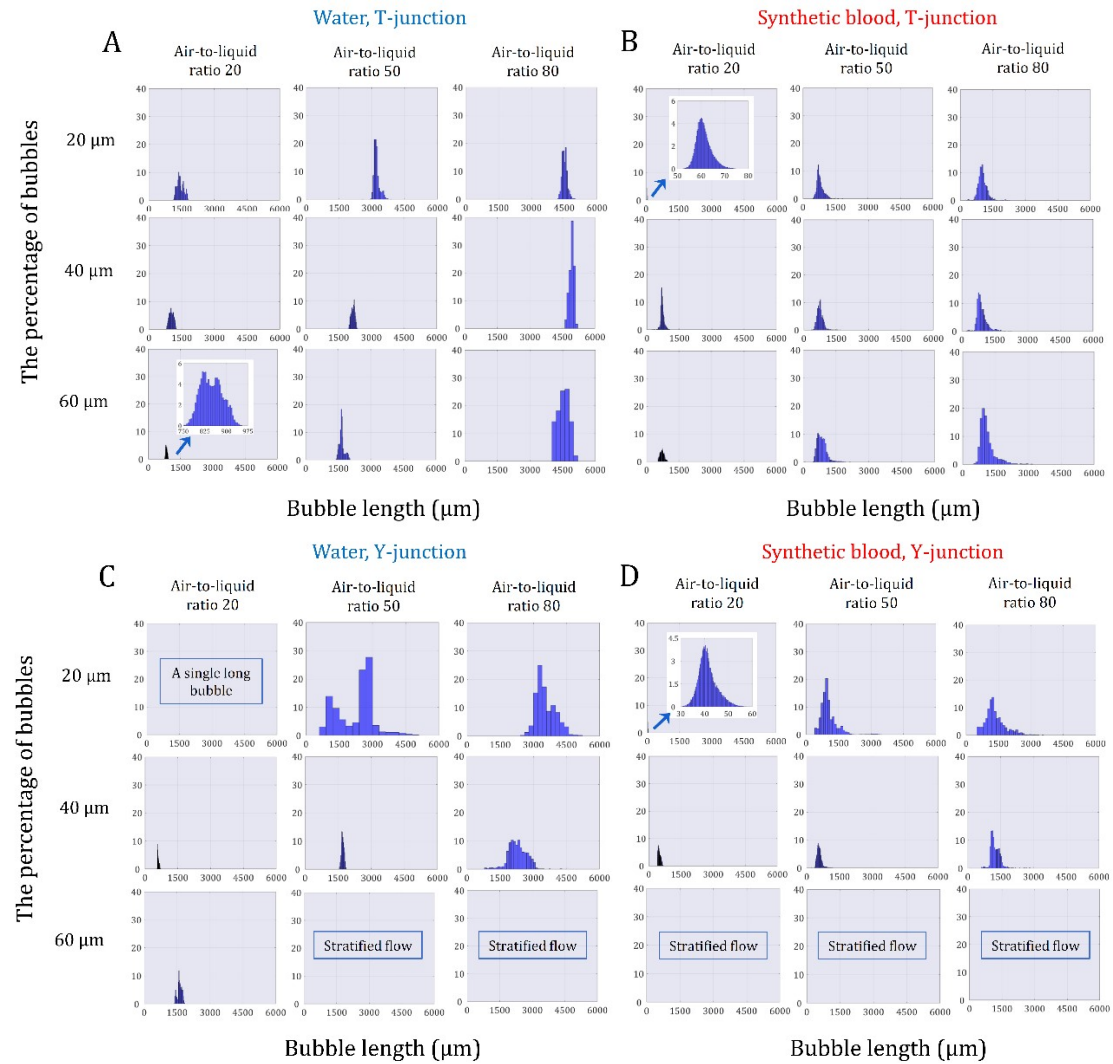
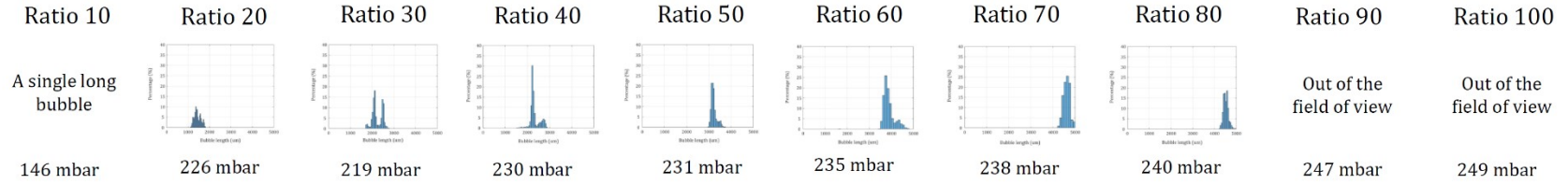
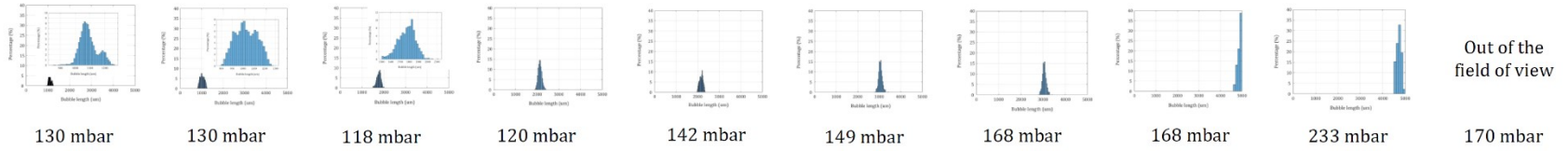


Fig. S15 Histograms of the bubble length in T- and Y-junctions channels for the selected ratios of 20, 50, and 80.

T-junction, Water, 20 μm



T-junction, Water, 40 μm



T-junction, Water, 60 μm

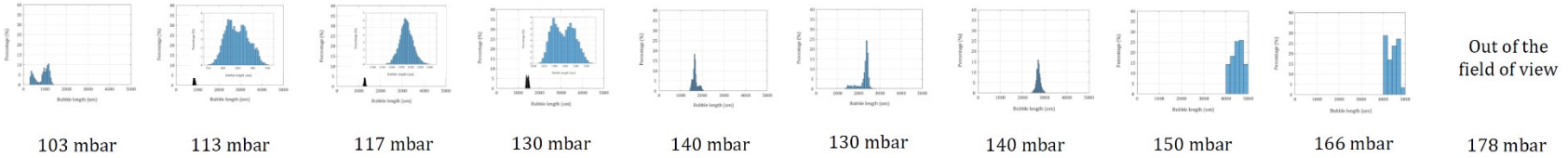


Fig. S16 Histograms of the bubble length in T-junction channels across different air-to-liquid ratios for the water.

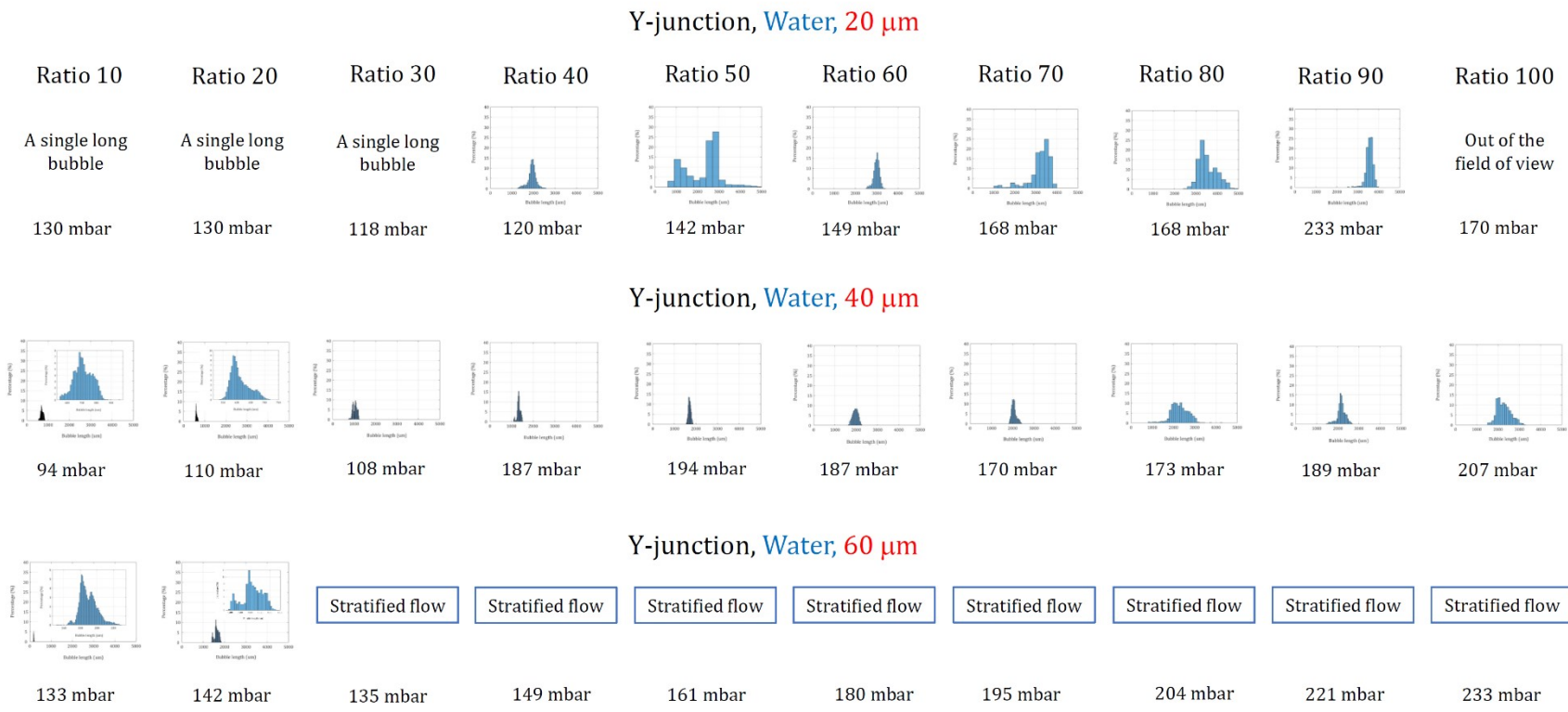
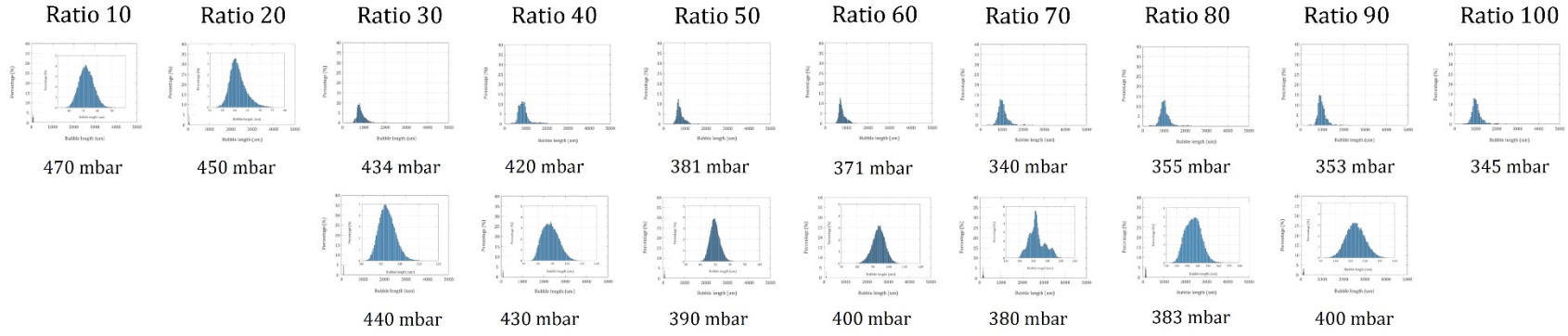


Fig. S17 Histograms of the bubble length in Y-junction channels across different air-to-liquid ratios for the water.

T-junction, Synthetic blood, 20 μm



Y-junction, Synthetic blood, 20 μm

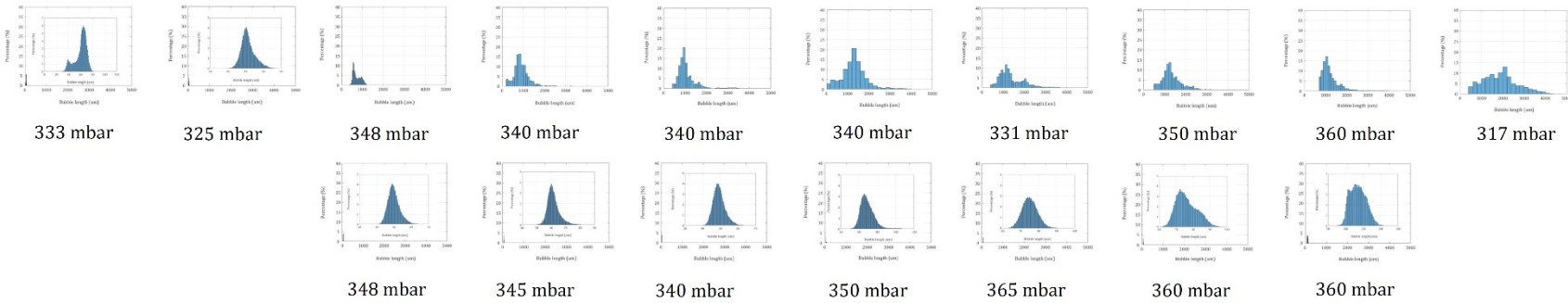
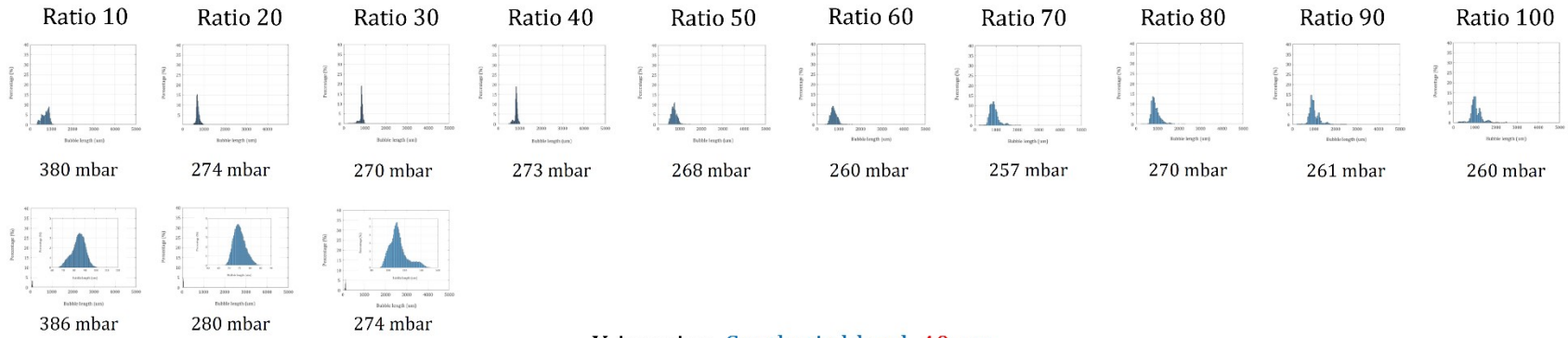


Fig. S18 Histograms of the bubble length in T-junction and Y-junction channels with 20 μm width across different air-to-liquid ratios for the synthetic blood.

T-junction, Synthetic blood, 40 μm



Y-junction, Synthetic blood, 40 μm

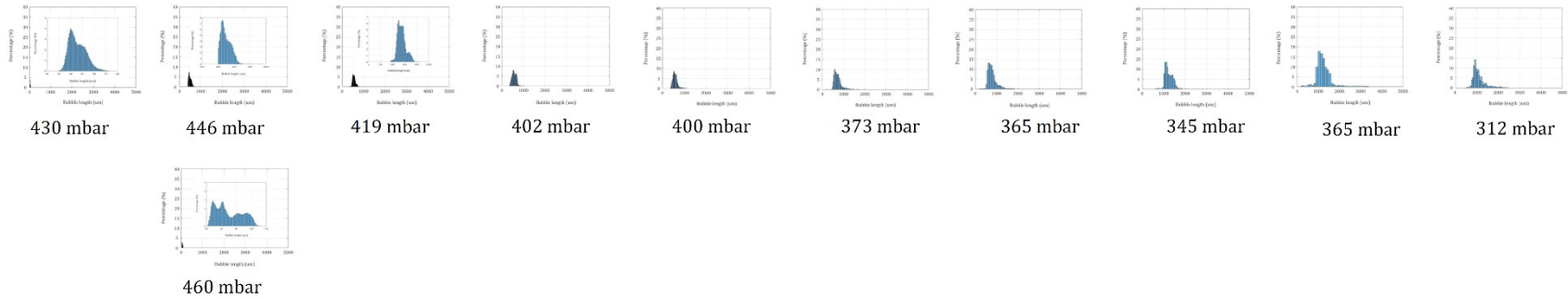
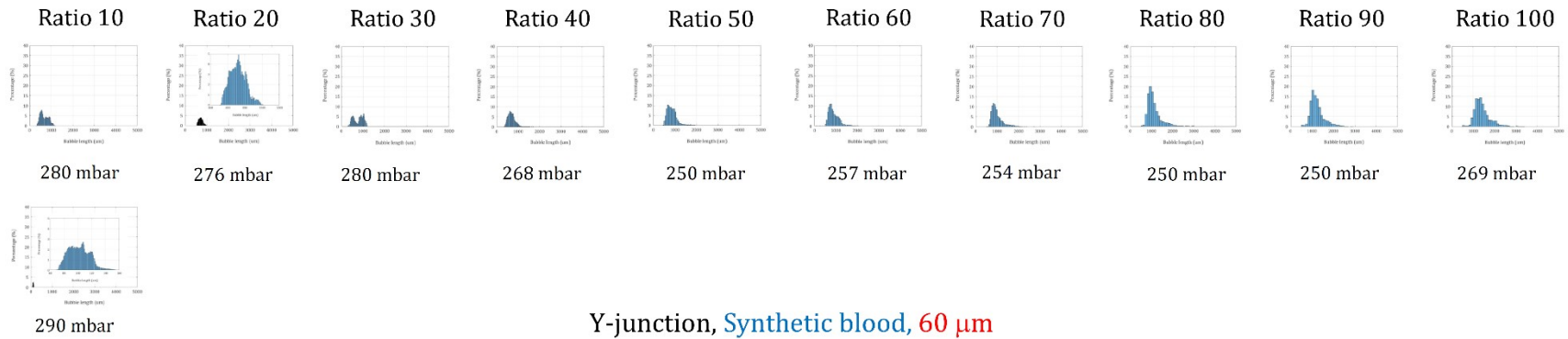


Fig. S19 Histograms of the bubble length in T-junction and Y-junction channels with 40 μm width across different air-to-liquid ratios for the synthetic blood.

T-junction, Synthetic blood, 60 μm



Y-junction, Synthetic blood, 60 μm

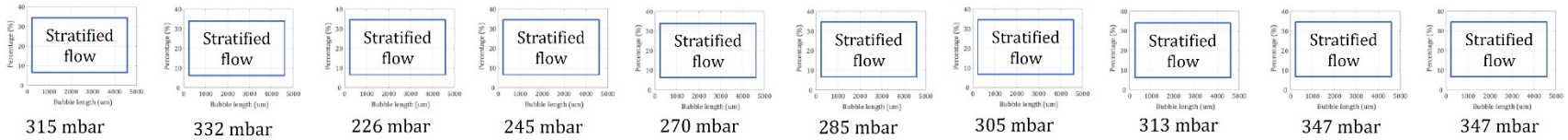


Fig. S20 Histograms of the bubble length in T-junction and Y-junction channels with 60 μm width across different air-to-liquid ratios for the synthetic blood.

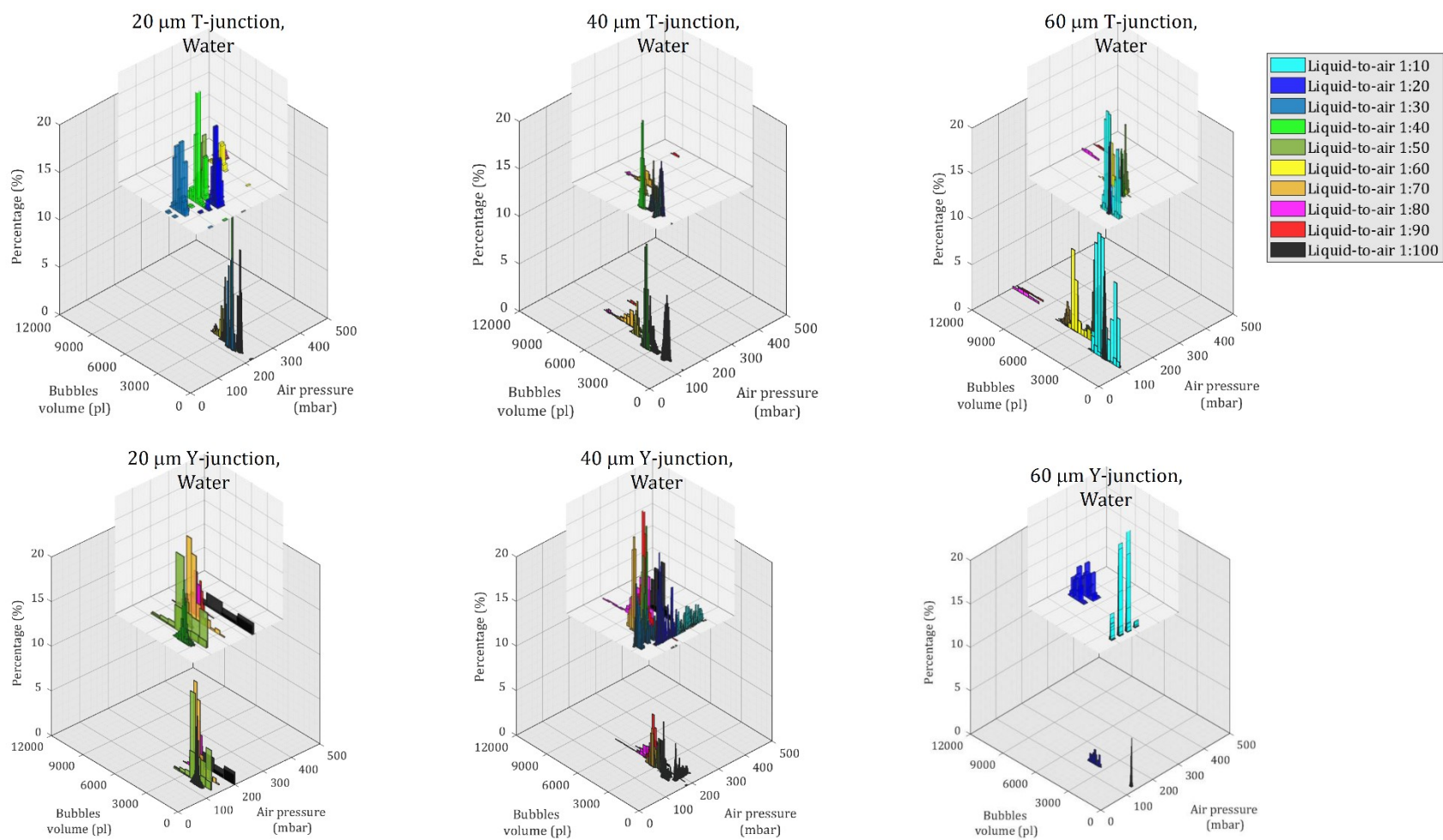


Fig. S21 Bivariate histograms depicts the relationship between bubble volume and air pressure at various air-to-liquid ratios in T- and Y-junction channels with water as the working fluid.

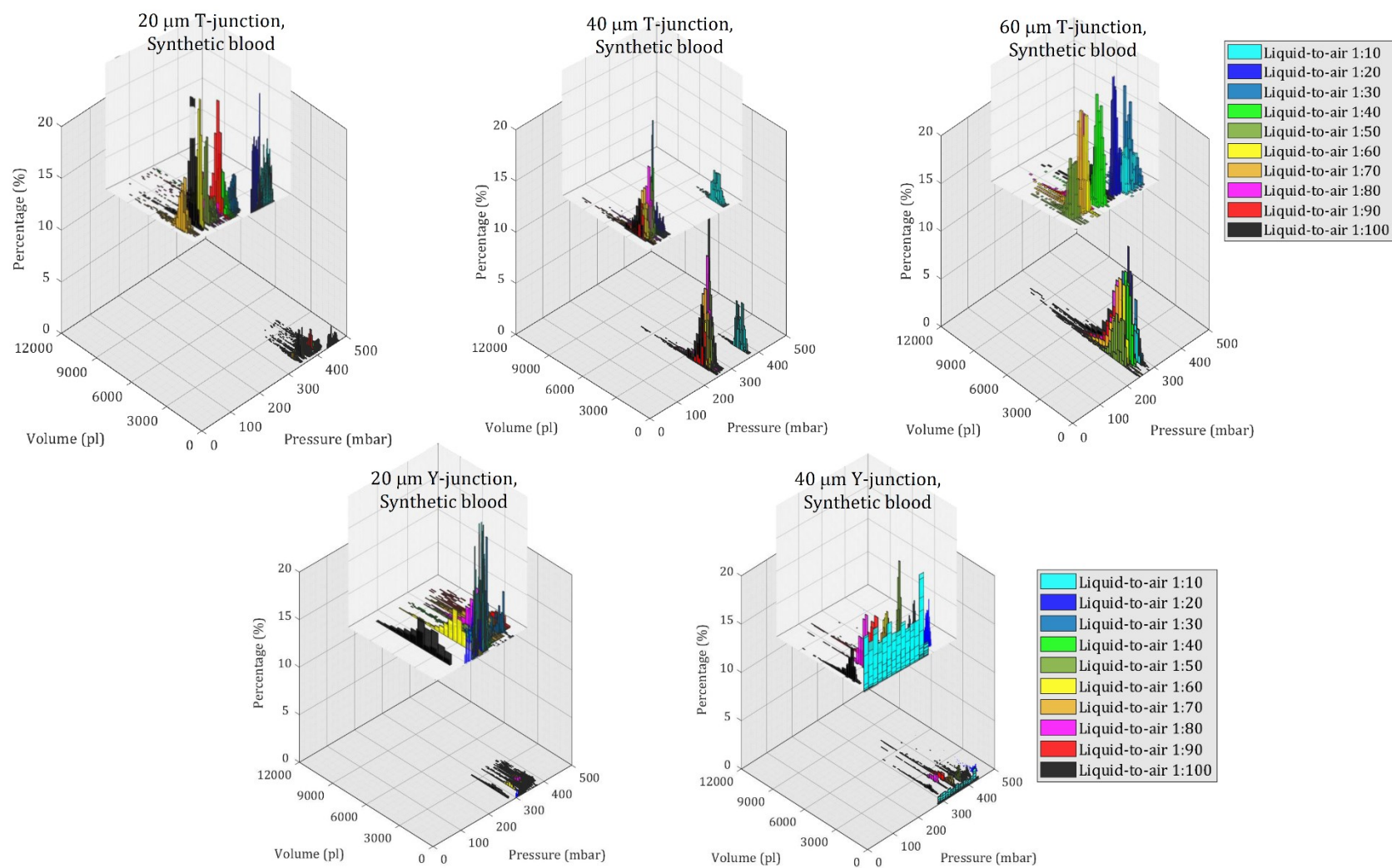


Fig. S22 Bivariate histograms depicts the relationship between bubble volume and air pressure at various air-to-liquid ratios in T- and Y-junction channels with synthetic blood as the working fluid.

9. Quantitative prediction of dimensionless numbers in extended channel widths

Considering the available dataset of dimensionless numbers obtained at various air-to-liquid ratios and channel widths, the development of a predictive function for estimating dimensionless numbers in larger channels proves to be a valuable tool for assessing the potential for gas embolism. This function relates a dimensionless number, such as Weber, Capillary, or the inverse form of Euler numbers, as a dependent variable to two independent variables: the air-to-liquid ratio and channel width. Using the curve fitting toolbox in MATLAB software, a fourth-order polynomial function demonstrates a suitable fit to the experimental data of these dimensionless numbers. This fit is assessed with respect to the coefficient of determination, denoted as R^2 .

$$\text{Dimensionless Number} = C_4R^4 + C_3R^3 + C_2R^2 + C_1R + C_0 \quad \text{Eq. 2}$$

$$C_i = A_{i1}d_H + A_{i2} \quad \text{Eq. 3}$$

where R is representative of the air-to-liquid ratio, while C_i (including C_4 , C_3 , C_2 , C_1 , and C_0) signifies the coefficients of a fourth-order polynomial. These coefficients are intricately linked to the channel width. Linear regression analysis revealed a perfect match between C_i and channel width using experimental data. A_{i1} and A_{i2} are responsible for denoting the first and second coefficients in this linear equation, respectively. Table S4 in the supplementary information provides the coefficients for the proposed functions associated with various dimensionless numbers. Furthermore, the MATLAB code included in the supplementary information was employed to perform the regression and extract the aforementioned coefficients.

Table S4. Coefficients of the dimensionless numbers relationships

		C ₄		C ₃		C ₂		C ₁		C ₀	
		C _i =A _{i1} d _H +A _{i2}		C _i =A _{i1} d _H +A _{i2}		C _i =A _{i1} d _H +A _{i2}		C _i =A _{i1} d _H +A _{i2}		C _i =A _{i1} d _H +A _{i2}	
Water	Capillary Number	A ₄₁	1.99E-11	A ₃₁	-3.57E-09	A ₂₁	2.10E-07	A ₁₁	-1.30E-06	A ₀₁	2.18E-06
		A ₄₂	-1.54E-09	A ₃₂	2.60E-07	A ₂₂	-1.37E-05	A ₁₂	2.31E-04	A ₀₂	2.08E-05
	(Euler Number) ⁻¹	A ₄₁	-4.63E-11	A ₃₁	7.81E-09	A ₂₁	-2.29E-07	A ₁₁	3.70E-06	A ₀₁	-6.41E-06
		A ₄₂	-4.72E-11	A ₃₂	7.52E-09	A ₂₂	-3.21E-06	A ₁₂	4.83E-05	A ₀₂	1.39E-04
	Weber Number	A ₄₁	-3.85E-13	A ₃₁	3.85E-11	A ₂₁	1.85E-09	A ₁₁	-3.53E-08	A ₀₁	8.61E-08
		A ₄₂	-1.78E-12	A ₃₂	9.13E-10	A ₂₂	-1.23E-07	A ₁₂	2.13E-06	A ₀₂	-1.30E-06
Synthetic blood	Capillary Number	A ₄₁	-4.72E-11	A ₃₁	1.12E-08	A ₂₁	-8.59E-07	A ₁₁	2.29E-05	A ₀₁	2.30E-05
		A ₄₂	-3.18E-11	A ₃₂	2.74E-08	A ₂₂	-5.41E-06	A ₁₂	3.46E-04	A ₀₂	-4.01E-04
	(Euler Number) ⁻¹	A ₄₁	-2.18E-12	A ₃₁	5.40E-10	A ₂₁	-4.44E-08	A ₁₁	1.30E-06	A ₀₁	5.18E-07
		A ₄₂	3.69E-11	A ₃₂	-8.57E-09	A ₂₂	6.31E-07	A ₁₂	-1.47E-05	A ₀₂	-1.40E-05
	Weber Number	A ₄₁	-1.37E-13	A ₃₁	3.44E-11	A ₂₁	-2.85E-09	A ₁₁	8.32E-08	A ₀₁	2.89E-08
		A ₄₂	2.13E-12	A ₃₂	-5.28E-10	A ₂₂	4.16E-08	A ₁₂	-1.08E-06	A ₀₂	6.59E-07

10. MATLAB code employed to perform the regression and extract the aforementioned coefficients

```
clc

% Set the font name and size
font_name = 'Cambria'; % Change to your desired font name
font_size = 18; % Change to your desired font size
% Set the font name and size for the axis numbers (tick labels)
font_name_axis = 'Cambria'; % Change to your desired font name
font_size_axis = 24; % Change to your desired font size
% Get the current axes handle
ax = gca;
% Set the font and font size for the current figure
set(gca, 'FontName', font_name, 'FontSize', font_size);

TW_ratio20 = [0 20 30 40 50 60 70 80];
TW_ratio40 = [0 10 20 30 40 50 60 70 80 90];
TW_ratio60 = [0 10 20 30 40 50 60 70 80 90];

TW_Weber20 = [0 3.22685E-06 5.72623E-06 7.40115E-06 1.20787E-05 2.93717E-05 3.68791E-05 3.63675E-05];
TW_Weber40 = [0 1.70012E-05 1.55141E-05 3.67985E-05 3.85376E-05 9.90227E-05 0.000178512 0.000209886
0.000289352 0.00037723];
TW_Weber60 = [0 6.80791E-06 2.87896E-05 6.57978E-05 8.95962E-05 0.000257327 0.000346525 0.000482736
0.00052912 0.000613177];

TW_Cap20 = [0 0.001362582 0.00181513 0.002063587 0.002636228 0.00411091 0.004606417 0.004574353];
TW_Cap40 = [0 0.002564671 0.002449934 0.003773169 0.003861304 0.006189547 0.008310457 0.00901121
0.010580463 0.012080768];
TW_Cap60 = [0 0.001485315 0.003054424 0.004617612 0.005388356 0.00913176 0.010596904 0.012507382
0.013094498 0.014096275];

TW_Eu20=[0 0.000186491 0.000387488 0.000446536 0.000848976 0.002112639 0.003217654 0.002935698];
TW_Eu40=[0 0.001012739 0.00092158 0.002902816 0.003002219 0.006769105 0.013025753 0.014878185
0.026067682 0.030758378];
TW_Eu60=[0 0.000430066 0.001830392 0.003950511 0.005316743 0.013770466 0.021797004 0.028642512
0.042097741 0.045405265];

T46p_ratio20 = [0 30 40 50 60 70 80 90 100];
T46p_ratio40 = [0 10 20 30 40 50 60 70 80 90 100];
T46p_ratio60 = [0 10 20 30 40 50 60 70 80 90 100];

T46p_Weber20 = [0 6.04884E-06 8.19823E-06 5.01072E-06 4.9535E-06 4.27728E-06 5.28102E-06 4.45698E-06
4.36609E-06];
T46p_Weber40 = [0 1.80509E-05 1.99552E-05 2.46678E-05 2.37694E-05 1.58328E-05 1.59051E-05 1.63199E-05
1.49535E-05 1.36293E-05 1.38292E-05];
T46p_Weber60 = [0 3.22782E-05 3.50218E-05 3.98565E-05 3.28944E-05 2.23126E-05 2.42658E-05 2.19764E-05
2.27132E-05 2.38509E-05 2.82211E-05];

T46p_Cap20 = [0 0.008724139 0.010156557 0.007940293 0.007894828 0.007336184 0.008151647 0.007488705
0.00741196];
T46p_Cap40 = [0 0.012358191 0.012993705 0.014446748 0.014181244 0.011574022 0.011600396 0.01175071
0.011248044 0.010738446 0.010816933];
T46p_Cap60 = [0 0.015124441 0.015754115 0.0168064 0.015268132 0.012574758 0.013113607 0.012479676
0.012687162 0.013001022 0.014142026];

T46p_Eu20=[0 0.000112542 0.000153802 0.000100057 0.000103018 9.28805E-05 0.000108086 8.51238E-05
9.15146E-05];
```

```

T46p_Eu40=[0 0.000310541 0.000383635 0.000492954 0.000471466 0.000317479 0.000327357 0.000326358
0.000282773 0.000263297 0.000268691];
T46p_Eu60=[0 0.000513807 0.000577667 0.000618211 0.000553374 0.000391736 0.000419995 0.000375876
0.000379061 0.000380158 0.000424233];

% Data for A = 20
R_20 = TW_ratio20;%
W_20 =TW_Cap20;%T46p_Cap20;%

% Data for A = 40
R_40 = TW_ratio40;%
W_40 =TW_Cap40;%T46p_Cap40;%

% Data for A = 60
R_60 = TW_ratio60;%
W_60 = TW_Cap60;%Weber60;%T46p_Cap60;%

% Define the input data for three values of A
A_values = [20, 40, 60];

% Perform linear regression for each set of data
coefficients_20 = polyfit(R_20, W_20, 4);
coefficients_40 = polyfit(R_40, W_40, 4);
coefficients_60 = polyfit(R_60, W_60, 4);
%=====
%Building coefficient matrix

COEFF=[coefficients_20;coefficients_40;coefficients_60];

COEFF_A=polyfit(A_values,COEFF(:,1),1);
COEFF_B=polyfit(A_values,COEFF(:,2),1);
COEFF_C=polyfit(A_values,COEFF(:,3),1);
COEFF_D=polyfit(A_values,COEFF(:,4),1);
COEFF_E=polyfit(A_values,COEFF(:,5),1);

% Data for A = 20
% Fit a fourth-order polynomial to the data
p_20 = polyfit(R_20, W_20, 4);
% Create a finer grid of R values for the fitted curve
R_fit = linspace(min(R_20), max(R_20), 1000);
% Evaluate the polynomial at the finer grid of R values
W_fit = polyval(p_20, R_fit);
% Plot the original data and the fitted curve
plot(R_20, W_20, 'r^', 'MarkerFaceColor', 'red', 'DisplayName', 'Experimental data for 20 um', 'MarkerSize', 10);
hold on
plot(R_fit, W_fit, '-r', 'DisplayName', 'Fitted curve for 20 um', 'LineWidth', 2);
grid on;

% Data for A = 40
% Fit a fourth-order polynomial to the data
p_40 = polyfit(R_40, W_40, 4);
% Create a finer grid of R values for the fitted curve
R_fit = linspace(min(R_40), max(R_40), 1000);
% Evaluate the polynomial at the finer grid of R values
W_fit = polyval(p_40, R_fit);
% Plot the original data and the fitted curve
plot(R_40, W_40, 'bs', 'MarkerFaceColor', 'blue', 'DisplayName', 'Experimental data for 40 um', 'MarkerSize', 10);
plot(R_fit, W_fit, '-b', 'DisplayName', 'Fitted curve for 40 um', 'LineWidth', 2);

% Data for A = 60
% Fit a fourth-order polynomial to the data

```

```

p_60 = polyfit(R_60, W_60, 4);
% Create a finer grid of R values for the fitted curve
R_fit = linspace(min(R_60), max(R_60), 1000);
% Evaluate the polynomial at the finer grid of R values
W_fit = polyval(p_60, R_fit);
% Plot the original data and the fitted curve
plot(R_60, W_60, 'go', 'MarkerFaceColor', 'green', 'DisplayName', 'Experimental data for 60 um', 'MarkerSize', 10);
plot(R_fit, W_fit, 'g', 'DisplayName', 'Fitted Curve for 60 um', 'LineWidth', 2);

A=200:300:2000;
R=0:1:100;

for i=1:length(A)
    for j=1:length(R)
        We(j)=((COEFF_A(1)*A(i)+COEFF_A(2))*R(j)^4)+((COEFF_B(1)*A(i)+COEFF_B(2))*R(j)^3)+((COEFF_C(1)*A(i)+COEFF_C(2))*R(j)^2)+((COEFF_D(1)*A(i)+COEFF_D(2))*R(j)^1)+((COEFF_E(1)*A(i)+COEFF_E(2)));
    end
    plot(R,We,'LineWidth', 2)
    hold on
end

% Calculate R2 for A = 20
W_fit_20 = polyval(p_20, R_20);
R2_20 = 1 - sum((W_20 - W_fit_20).^2) / sum((W_20 - mean(W_20)).^2);

% Calculate R2 for A = 40
W_fit_40 = polyval(p_40, R_40);
R2_40 = 1 - sum((W_40 - W_fit_40).^2) / sum((W_40 - mean(W_40)).^2);

% Calculate R2 for A = 60
W_fit_60 = polyval(p_60, R_60);
R2_60 = 1 - sum((W_60 - W_fit_60).^2) / sum((W_60 - mean(W_60)).^2);

% Display R2 values
fprintf('R-squared (R2) values:\n');
fprintf('A = 20: R2 = %.4f\n', R2_20);
fprintf('A = 40: R2 = %.4f\n', R2_40);
fprintf('A = 60: R2 = %.4f\n', R2_60);

syms A R We_sym
% Create symbolic expressions for the coefficients and round them to a specific number of decimal places
decimal_places = 4; % Adjust this to your desired number of decimal places
a = vpa(COEFF_A(1), decimal_places);
b = vpa(COEFF_B(1), decimal_places);
c = vpa(COEFF_C(1), decimal_places);
d = vpa(COEFF_D(1), decimal_places);
e = vpa(COEFF_E(1), decimal_places);

% Define the symbolic expression for We
We_sym = (a * A + COEFF_A(2)) * R^4 + (b * A + COEFF_B(2)) * R^3 + (c * A + COEFF_C(2)) * R^2 + (d * A + COEFF_D(2)) * R + (e * A + COEFF_E(2));
% Display the symbolic expression
disp(['We = ', char(We_sym)]);

```

References

1. K. Subramani, in *Emerging nanotechnologies for manufacturing*, Elsevier, 2015, pp. 279-293.
2. K. Brookshier and J. Tarbell, *Biorheology*, 1993, **30**, 107-116.
3. L. Webb, *The Pegasus Review: UCF Undergraduate Research Journal*, 2020, **12**, 6.
4. R. E. Wells and E. W. Merrill, *The Journal of clinical investigation*, 1962, **41**, 1591-1598.
5. M. A. Elblbesy, *AIMS Biophysics*, 2019, **6**, 39-46.
6. H. N. Harkins and W. D. Harkins, *The Journal of Clinical Investigation*, 1929, **7**, 263-281.
7. R. S. Abiev, *Chemical engineering journal*, 2013, **227**, 66-79.
8. S. Molla, D. Eskin and F. Mostowfi, *Lab on a Chip*, 2011, **11**, 1968-1978.
9. R. Zhang, F. Tao, H. Jin, X. Guo, G. He, L. Ma, R. Zhang, Q. Gu and S. Yang, *Processes*, 2022, **10**, 799.
10. M. Akbari, D. Sinton and M. Bahrami, 2009.
11. Y. Yin, C. Zhu, R. Guo, T. Fu and Y. Ma, *International Journal of Heat and Mass Transfer*, 2018, **127**, 484-496.